

313099

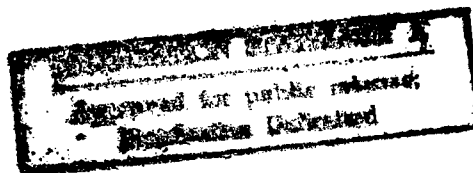
JPRS-CST-84-030

10 October 1984

China Report

SCIENCE AND TECHNOLOGY

19981020 130



DTIC QUALITY INSPECTED 3

FBIS

FOREIGN BROADCAST INFORMATION SERVICE

REPRODUCED BY
NATIONAL TECHNICAL
INFORMATION SERVICE
U.S. DEPARTMENT OF COMMERCE
SPRINGFIELD, VA. 22161

5
49
A03

NOTE

JPRS publications contain information primarily from foreign newspapers, periodicals and books, but also from news agency transmissions and broadcasts. Materials from foreign-language sources are translated; those from English-language sources are transcribed or reprinted, with the original phrasing and other characteristics retained.

Headlines, editorial reports, and material enclosed in brackets [] are supplied by JPRS. Processing indicators such as [Text] or [Excerpt] in the first line of each item, or following the last line of a brief, indicate how the original information was processed. Where no processing indicator is given, the information was summarized or extracted.

Unfamiliar names rendered phonetically or transliterated are enclosed in parentheses. Words or names preceded by a question mark and enclosed in parentheses were not clear in the original but have been supplied as appropriate in context. Other unattributed parenthetical notes within the body of an item originate with the source. Times within items are as given by source.

The contents of this publication in no way represent the policies, views or attitudes of the U.S. Government.

PROCUREMENT OF PUBLICATIONS

JPRS publications may be ordered from the National Technical Information Service, Springfield, Virginia 22161. In ordering, it is recommended that the JPRS number, title, date and author, if applicable, of publication be cited.

Current JPRS publications are announced in Government Reports Announcements issued semi-monthly by the National Technical Information Service, and are listed in the Monthly Catalog of U.S. Government Publications issued by the Superintendent of Documents, U.S. Government Printing Office, Washington, D.C. 20402.

Correspondence pertaining to matters other than procurement may be addressed to Joint Publications Research Service, 1000 North Glebe Road, Arlington, Virginia 22201.

10 October 1984

CHINA REPORT
SCIENCE AND TECHNOLOGY

CONTENTS

PEOPLE'S REPUBLIC OF CHINA

APPLIED SCIENCES

Physical Startup of High-Flux Engineering Test Reactor (Peng Feng; HE KEXUE YU GONGCHENG [CHINESE JOURNAL OF NUCLEAR SCIENCE AND ENGINEERING], No 1, Mar 83).....	1
Equipment for Recovery of Entrained Organic Matter From Raffinate in Solvent Extraction of Uranium (Teng Yuanxun, Liu Min; HE KEXUE YU GONGCHENG [CHINESE JOURNAL OF NUCLEAR SCIENCE AND ENGINEERING], No 1, Mar 83).....	17
Nation Said To Rank High With 15 Satellites (XINHUA, 5 Sep 84).....	27
Report on National Tungsten-Molybdenum Conference (Tang Xuwen; GANGTIE [IRON AND STEEL], No 10, 1983).....	28
Protecting Civil Air Defense Installations From Seepage (Liu Zhongyi; DIXIA GONGCHENG [UNDERGROUND ENGINEERING], No 10, 1983).....	30
Experimental Investigation of Crippling Strength of Chinese Aluminum Alloy (LY12CZ) Sections (Zhang Fubao; FUDAN XUEBAO-ZIRAN KEXUE BAN [FUDAN JOURNAL--NATURAL SCIENCES EDITION], No 4, 1983).....	32
International Conference on Rare Earth Development and Applications and International Fair for Rare Earths and Their Application Products (ZHONGGUO XITU XUEBAO [JOURNAL OF THE CHINESE RARE EARTH SOCIETY], No 1, 1984).....	38

LIFE SCIENCES

Better Food, Healthcare Increase Average Size
(XINHUA, 7 Sep 84)..... 41

Briefs

Nei Mongol Medical Conference 42

ABSTRACTS

ASTRONAUTICS

YUHANG XUEBAO [JOURNAL OF THE CHINESE SOCIETY OF ASTRONAUTICS],
No 2, 30 Apr 84)..... 43

PHYSICAL STARTUP OF HIGH-FLUX ENGINEERING TEST REACTOR

Beijing HE KEXUE YU GONGCHENG [CHINESE JOURNAL OF NUCLEAR SCIENCE AND ENGINEERING] in Chinese No 1, Mar 83 pp 11-22

[Article by Peng Feng [1756 7685] of the Physics Laboratory of the Engineering Test Reactor Research Institute at the Southwest Reactor Engineering Research and Design Institute]

[Text] Abstract

Physical startup of the High-Flux Engineering Test Reactor (HFETR) was completed in 1980. Many physical parameters have been measured since then, including reactor criticality, control rod efficiency, component reactivities, reactivity coefficients, relative flux distributions and absolute values of fast and thermal neutrons, parameters of neutron spectrum, gamma dose distribution in the core, dynamic reactor parameters, etc.

The information obtained is valuable not only for safe reactor operation, isotope production, materials testing and fuel irradiation, but also for improvement on physical and shielding design for HFETR.

I. Introduction

After criticality was achieved in the high-flux engineering test reactor (HFETR) constructed by the Southwest Reactor Engineering Research and Design Institute in 1979, a physical startup was carried out in 1980. It is a pressurized-water reactor that uses high-concentration uranium fuel and has a metallic beryllium reflecting layer.

There are special characteristics in the physical startup of high-flux reactors. The probe efficiency of control and protection systems will be fairly low if the geometric dimensions of the reactor core are too small; there is a fairly large difference between control rod efficiency and element box reactivity equivalents; it is hard to approach certain places in the active section. Measures should be taken to overcome these difficulties in experiments. In order to carry out systematic measurement of the physical parameters

of the reactor, to improve the precision of experiments, and to reduce work time, we still must develop and debug several experimental instruments and detection instruments, and we should study several new experimental methods.

Physical startup provides information on reactor power increases, safe operation, materials irradiation, element testing and isotope production. It is also a test of the reactor's physical shield design.

II. A Brief Description of the Components in the Active Region of a High-Flux Engineering Test Reactor

The structure of a high-flux reactor is described in source 1. The elements are multilayer thin-wall pipe sets. The common elements are six layers of fuel pipes having a wall thickness of 1.5 mm. There is a 2 mm water gap between them. The follower element is a four-layer fuel pipe group with dimensions identical to the corresponding four layers of common elements. The U-235 used is 90 percent enriched. Each element contains 270 grams of U-235 (the following elements have 117 grams). The active section is 1,000 mm high. The outside diameter of the element box is 63 mm.

The beryllium and aluminum blocks are regular hexagons 62.5 mm across. There is a 20 mm diameter hole in the center of the beryllium blocks.

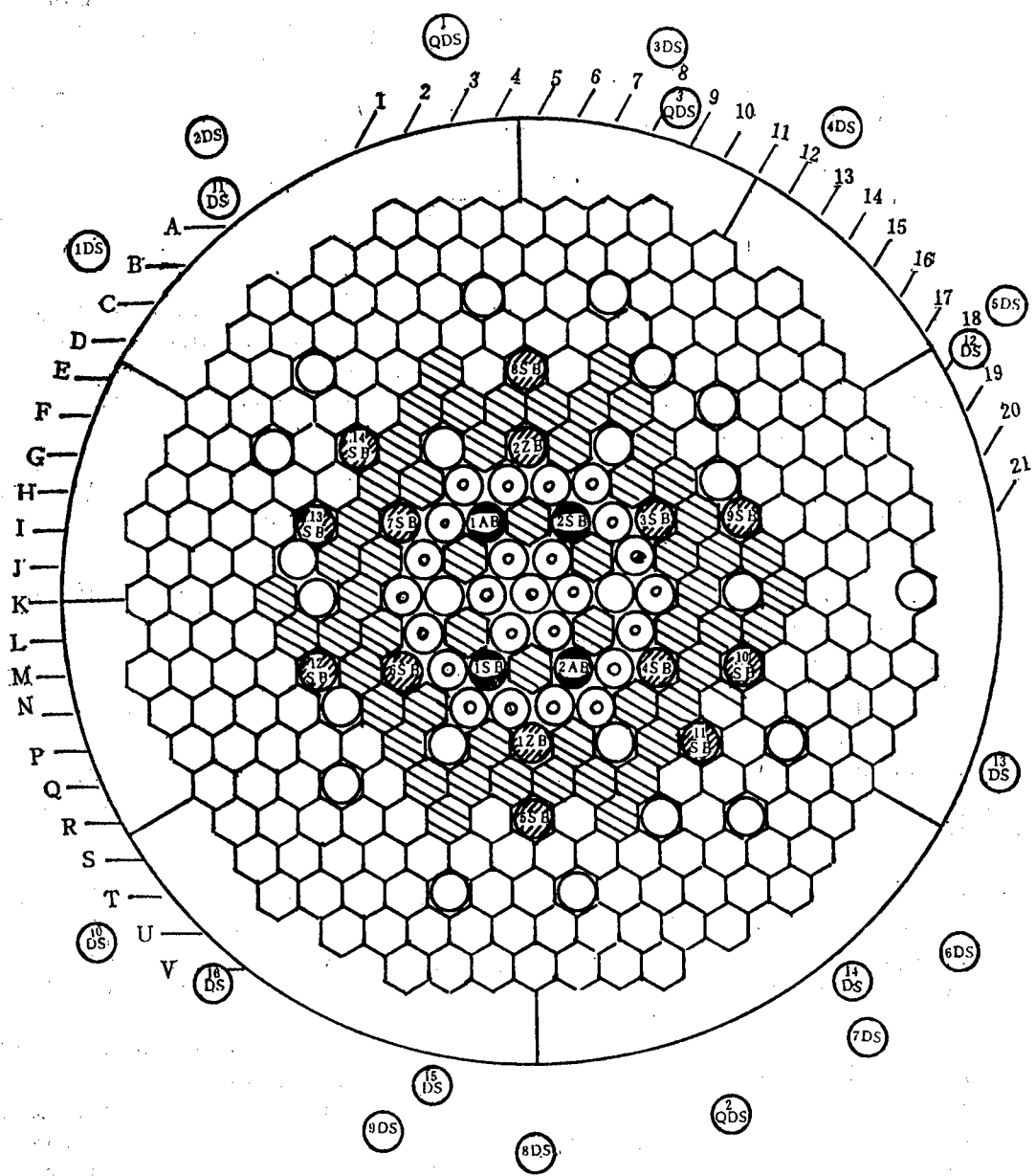
The control rods are organized as an absorber, a follower and a transitional stage linking the two. The absorber is made of silver-indium-cadmium alloy and the transitional stage is made of boron steel. Apart from the follower element, the other type of follower is 51 mm diameter beryllium rod. Stainless steel is used in the absorbers and transitional stage in the automatic regulation rods.

There are 10 isotope targets and one materials irradiation tank installed in the first active section. A beryllium rod or irradiation sample 17 mm in diameter is installed in the central hole of the beryllium blocks. An irradiation experiment duct can be placed outside the beryllium reflection layer.

A thermometric thermocouple, a flow pressure measurer pipe and a helical long vanadium neutron self-supply capacity detector are installed in an element in the center of the active region. The two adjacent elements contain pneumatic activator ball pipes. Twelve 63 mm diameter incidental ducts are placed around the active section at the time of physical startup, and various types of detectors can be installed in them. The neutron source at startup has a strength of 2×10^7 n/sec.

III. Criticality Experiments

Figure 1 shows the arrangement of the active region during the first criticality experiment. The reactor contains a total of 25 elements, and two follower elements are normally in the active section. There is a total of 7 kg of U-235. There also are six beryllium blocks and two isotope targets within the active section. The reflection layer has 51 beryllium blocks and 8 isotope targets. The neutron source is located at K20. The placement of the detectors is shown in Table 1.



Key:

○ Element	● Control rod (with element)	◆ Beryllium
○ Duct, target	● Control rod (with beryllium)	○ Aluminum

Figure 1. Reactor Core Layout at First Criticality

Table 1. Instrumentation Used for Physical Startup

<u>Instrument name</u>	<u>Model</u>	<u>Number</u>	<u>Detector position</u>
Counting tube neutron measuring system	KY1901	2	C6, T16
Fission chamber neutron measuring system	KY1902	2	C9, T13
Ionization chamber neutron measuring system	KY1903	1	R17
Sounding apparatus	KY540 DG1	1	E3
Pulsed neutron tube	Special	1	E11
Pulse counting apparatus	KY540 DG1	1	J5
Power measurement system	Special	2	F13, Q9
Power protection system	Special	2	G3, P19
Small power protection system	Special	2	3QDS, 14DS
Water level gauge within reactor	Special	1	R19
Gamma dose rate gauge	FJ 344	1	Upper part of active section

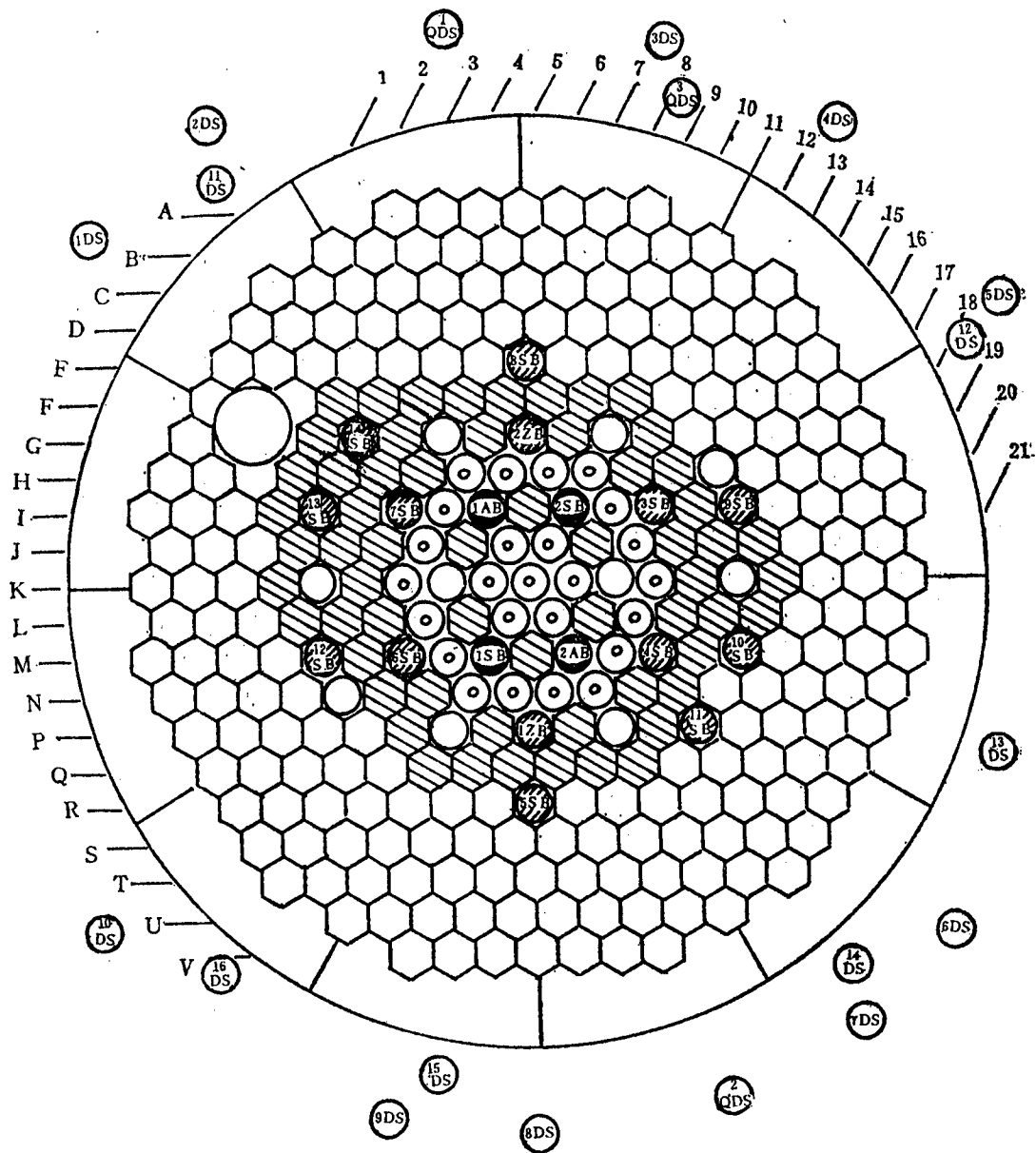
To guarantee safety at first criticality, water was first added intermittently when approaching criticality. The remaining elements and beryllium blocks were then added gradually according to the extrapolated values in order to attain the present arrangement. The rods were then raised gradually to attain criticality. Moreover, the pulse neutron method and the source multiplier method were used to premeasure the equivalent and efficiency curve of the raised rods. Criticality is extrapolated from the reactivity equivalent from each addition and not simply according to the height to which the rods are raised.

The number of startup meters was reduced during each of the later criticality experiments. In the end, the criticality duct was removed, and criticality was achieved by raising the rods directly.

After the first criticality, the position of the reactor core was readjusted and the irradiation experiment duct was installed. There was a total of 54 beryllium blocks. The arrangement of the reactor core is shown in Figure 2. A restartup criticality experiment was conducted.

The material in the enclosures of the control rod absorbers was changed to 1 mm thick stainless steel during the low power criticality experiments (it originally was 0.5 mm thick aluminum), and stability was maintained in the arrangement of the reactor core. Finally, a criticality experiment was carried out at increased power.

The results of each criticality experiment are shown in Table 2. Theoretical analysis shows that the greatest difference in the rod positions at criticality are primarily due to the internal arrangement of the pile and differences in water temperature.²



Key:

- Element
- Control rod (with element)
- ▨ Beryllium
- Duct, target
- ▨ Control rod (with beryllium)
- Aluminum (with beryllium)

Figure 2. Reactor Core Layout at Restartup

Table 2. Results of Criticality Tests

Test	Water temperature (°C)	Rod position at critical (mm)					
		3SB	6SB	1,2AB	1,2ZB	7SB	1,2,4, 7SB
First criticality	15	290	0	900	0	0	1000
	15	180	180	900	0	0	1000
Restartup criticality	23	448	0	900	0	0	1000
Low power							
Criticality	18	284	284	900	0	0	1000
Increased power criticality	23	275	275	900	0	0	1000

Note: Control rod codes are: (1) AB--Safety rod, (2) SB--manual supplementary rod, and (3) ZB--Automatic regulation rod

IV. Measurement of the Physical Parameters of the Reactor

1. Measurement of the efficiency of cold control rods

Measurement of the efficiency of the control rods was mainly carried out using an FMJ-3 reactive measurement modeling computer. Moreover, a well-graduated 1ZB was commonly used for relative measurements, and testing was done using the periodic method and pulse neutron method.

When a simulator was used for the measurements, a detector was installed at a nearby position at the "node" of minimum changes in flux based on the calculated value of the stability of flux distribution before and after the rods were lowered. Locational effects on the measurements were thus avoided. Consideration was given to the influence of the delayed photoneutrons from the beryllium in the installation of delayed neutron parameters. The results of the measurements are shown in Table 3.

Table 3. Cold Control Rod Efficiency

Control rods	Measurement conditions	Efficiency (β_{eff})		
		Simulator method	Graduated method	Calculation method
1,2AB	All other rods inserted	14.0	--	14.6
2AB	1AB pulled out	6.5	--	6.2
1SB	2AB pulled out	--	9.0	8.9
2SB	As above	--	7.0	--
3SB or 6SB	1,2AB pulled out	1.40	--	1.38
4SB or 7SB	As above	2.30	2.36	2.40
1ZB	As above	0.87	--	0.82
Peak reactor depth	All rods inserted	16.0	--	16.6

There is a 5 percent measurement error in control rod efficiency. It can be seen from Table 3 that there is an obvious interference effect between the control rods.

2. Measurement of component reactivity equivalents

Component reactivity equivalents were measured using the pulsed neutron method. Depending on the different degrees of criticality, the pulse repetition frequency was 15 to 200 Hz, the track width was 500 to 30 μ s, and the width of the pulse was 500 to 300 μ s. A 4096 track Model FH450 amplitude analyzer (working in a 127 track configuration) was used to record pulsed neutron responses. The measurements were taken by insertion during the criticality experiments, with 21 elements and 49 beryllium blocks in the pile. The criticality value of the measurement components was measured first within the pile, and the components that were measured were then taken out. Secondary criticality of the pile was measured using the pulsed neutron method, thereby deriving the reactivity equivalent of the measured components. The data was processed in a DJS-6 by compilation procedures. The results are shown in Table 4, and the measurements have a 5 percent error.

Table 4. Component Reactivity Equivalents

Component name	Position	Reactivity equivalent (β eff)
Element	J10 or K12	4.5
Element	K11	3.4
Element	H8	2.2
Element	K14	1.5
Element	N11	0.8
Beryllium	J9	1.8
Beryllium	P14	0.62
Beryllium	H13	0.09

3. Measurement of automatically regulated thermal rod efficiency

A simulator was used to measure the thermal rod efficiency of the 1ZB after power was increased, and it was also used to graduate the remaining control rods. There were changes in temperature and xenon poisons due to reactor power at the time of thermal rod graduation, so there must be corresponding correction of the results provided by the simulator. We discovered that excellent results could be obtained by extrapolating from the curve of measured values according to the curve of the drop in reactor power, and correcting the temperature feedback. Moreover, because of the serious xenon poisoning in the high-flux reactor, we used the uniform medium poisoning formula to correct the estimate of xenon poisoning during the process of rod withdrawal, and also obtained satisfying results. The measurement error in thermal rod efficiency was 10 percent after the above revisions were made.

Under conditions of 50 percent reactor power and balanced xenon, the total efficiency of the 1ZB was measured as 0.90 β_{eff} , and the linear section

differential efficiency was $0.016 \beta_{\text{eff}}/\text{cm}$. This corresponds to the range of error from theoretically calculated results.²

4. Measurement of temperature coefficients and transient power coefficients

Using the main pump of the reactor to increase the temperature caused a gradual rise in the water temperature within the reactor. The temperature coefficient α_T^m of the degraded agent was measured under conditions of no neutron poisoning and no burnup. The result obtained was:

$$\alpha_T^m = - (0.51 + 0.027T) \times 10^{-4} \frac{\Delta K}{K} / {}^\circ C$$

The temperature coefficient α_T was measured under powered conditions. Under conditions of unchanged reactor power and a single loop flow rate, the method of reduced double loop effective heat exchange flow caused the temperature in the reactor to rise greatly. The changes in reactivity were measured, and xenon poisoning was corrected. The results obtained were:

$$\alpha_T = - 1.1 \times 10^{-4} \frac{\Delta K}{K} / {}^\circ C$$

The average temperature of the active region during the experiment was $35 {}^\circ C$.

The transient power coefficient α_p of the reactor was measured. It is defined as the reactive change engendered by a change of 1 MW in reactor power due to the temperature effects of reactor acceleration. After the reactor power was raised to a certain level during the experiment, a simulator was used to graduate a control rod. Because the rod being measured had been lowered, there was a subsequent drop in reactor power. The search for the temperature feedback reactivity Δ_{pT} corresponding to the drop in power ΔN was derived as:

$$\alpha_p = \frac{\Delta_{pT}}{\Delta N}$$

Under conditions of 50 percent power, balanced xenon and a flow of 2,400 t/h, the result was:

$$\alpha_p = - 1.25 \times 10^{-4} \frac{\Delta K}{K} / {}^\circ C$$

5. Measurement of undelayed neutron decay constants

A CNF-1 cross-correlated noise analyzer was used to measure the power spectral density under zero power conditions. Two BF3 neutron counting tubes were placed at the D6 and S16 positions. Spectral analysis was done after a tape recorder was used to record the signals. The results are shown in Figure 3. After being processed using the method of least squares, the undelayed neutron decay constant value α_c was obtained. The pulse neutron method was used to measure this value α_c and the calculated value, as shown in Table 5.

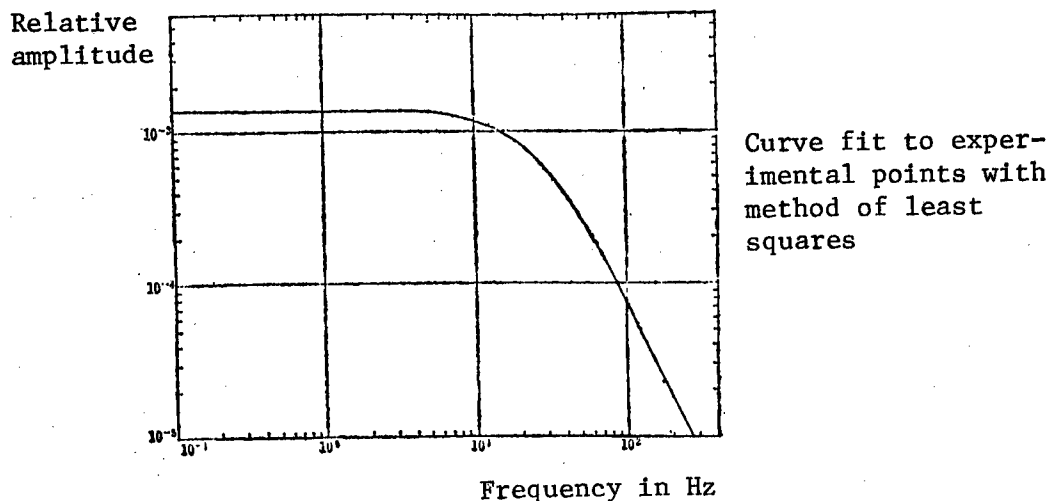


Figure 3. No-power Spectral Density

Table 5. Undelayed Neutron Decay Constants

Test Method	$\alpha_c (5^{-1})$
Pulsed neutron method	146±7
Interrelationship method	149±7
Calculated value	168

V. Measurement of Gamma Dose Field Distribution

At the zero power stage, a thermal release photo dosimeter (TLD) was used to measure the gamma dose field distribution within the reactor. The dimensions of the LiF(MgTiNa) thermal photon release element were $1 \times 1 \times 6 \text{ mm}^3$, and it had an Li-7 content of 99.99 percent. The material used in the heating box was polytetrafluoroethylene. The outside diameter of the box was 9.5 mm, the wall thickness was 4 mm and it was 40 mm long. Because equilibrium in delayed gamma in the fission products within the reactor had not yet been reached at the time of exposure, the calculation of this item was corrected to 14 percent. The greatest thermal neutron response of the thermal photo release element was 3 percent.

In the low power stage, measurements were made using a model DLS-204 reactor core gamma ionization chamber. The outer diameter of the gamma ionization chamber was 32 mm, the length was 180 mm, and the sensitive region was 80 mm long. Readings were taken using a ten-duct gamma measurer.

The error between the two measurement methods was 20 percent. The radial and axial gamma dose rate distributions are shown in Tables 6 and 7. The experimental and theoretical values of the radial distribution corresponded quite well. The axial distribution conformed fairly well in the position of the K11 element box, and the calculated value at the E11 incidental duct was derived

Table 6. Radial Gamma Dose Distribution

Component	Position	Dis- tance chamber (mm)	Gamma dose rate (R/w/h)			
			Gamma ion- ization element h = 500	Thermal release element h = 510	Calcu- lated I, (4) h = 500	Calcu- lated II, (4) h = 500
Element	K11	0	--	250 (h=490)	280	230
Element	K12	64	--	220	230	172
Element	K14	192	--	104	140	87
Beryllium	K15	256	--	38	71	55
Beryllium	K17	384	--	12	20	13
Temporary conduit	E11	384	8.2	--	--	13
Irradiation test duct	F2-G2-G3	480	3.0	6.7 (h=300)	--	4.9 (h=440)
Ionization chamber duct	14DS	760	0.36	--	--	0.55
As above	9DS	1273	0.0014	--	--	0.001

Note: h refers to the height of the active section (in mm).

Table 7. Axial Gamma Dose Distribution

Component	Position	Axial height (mm)	Gamma dose rate (R/w/h)		
			Gamma ionization chamber	Thermal release element	Calculated value II (4)
Element	K11	70	--	152	89
Element	K11	210	--	162	154
Element	K11	490	--	250	226
Element	K11	910	--	78	96
Temporary conduit	E11	35	3.5	--	4.0
Temporary conduit	E11	575	7.2	--	13.1
Temporary conduit	E11	1000	2.2	--	0.33
Temporary conduit	E11	2000	0.14	--	0.0002

by multiplying the axial distributional increase by the radial decrease in the reactor center. They were highly similar. Moreover, because of the "conduit effect" of the duct, the experimental value was obviously high after the axial height exceeded 1 meter.

VI. Measurement of the Neutron Energy Spectrum and Fast Neutron Flux

This measurement technique of detection plate activation was used in the measurement of the neutron energy spectrum and flux. The detection plate parameters that were used are shown in Table 8.

Table 8. Activated Detection Plate Parameters

Name of detection plate	Use	Dimensions (mm)	Weight (mg)	Materials purity or components (percent)	Activated nucleus (percent)	Activity (per cent)	Product	Half life
Nickel plate	Rapid spectral measurement	6	87.62	99.99	Ni58	67.88	Co53	71.3d
" "	Rapid flux measurement	7	58.6	99.99	Ni58	67.88	Co53	71.3d
Iron plate	Rapid spectral measurement	6	119.5	99.995	Fe56	91.6	Mn56	2.578h
	As above	6	"	"	Fe54	5.82	Mn54	312.5d
Indium plate	As above	6	55.76	99.999	In115	95.72	In115	4.486h
Aluminum plate	As above	6	40.23	99.999	Al127	100	Na24	15h
Zinc plate	As above	6	102.4	99.999	Zn64	48.9	Cu64	12.71h
Titanium plate	As above	6	144.4	99.9993	Ti46	7.93	Sc46	83.34d
" "	As above	"	"	"	Ti47	7.28	Sc47	81.6h
" "	As above	"	"	"	Ti48	73.94	Sc48	44h
Magnesium plate	As above	6	23.6	99.999	Mg24	78.99	Na24	15h
Manganese plate	Thermal flux measurement	3x10 two ends, R1.5	60.3	Mn=80, Ni=20	Mn55	100	Mn56	2.578h
" "	Superthermal flux measurement	8	42	"	"	"	"	"
Gold plate	Absolute thermal flux measurement	5	12.5	99.999	Au197	100	Au198	2.696d
" "	Super thermal flux measurement	7	81	"	"	"	"	"
Lutetium plate	Neutron temperature measurement	8	24.4	Lu=9.8, Mn=4.1	Lu176	0.026	Lu177	6.71d

1. Measurement of fast neutron spectral energy

A total of seven types of threshold detectors were employed: nickel, iron, indium, aluminum, titanium, zinc and magnesium. Their activation response overlap zone was 1 to 12 MeV. Measurements of activity were made with a Scorpio-3000 germanium-lithium gamma spectrometer. After the mononuclear activation rate was obtained, the well-edited SAND-II, RDMM and other procedures were used for processing. Table 9 shows the fast neutron integral flux neutron energy levels of greater than 1 MeV.

Table 9. Rapid Neutron Integral Flux

Component	Position	Axial height (mm)	Reactor power (MW)	Irradiation time (min.)	Fuel consumption (MWd)	En>1 MeV rapid integral flux ($\times 10^{11}$ n/cm ² /s)		Relative flux	Method
						SAND-II method	RDMM method		
Element	L12	400	0.08	120	0	6.9	6.8	6.7	
Beryllium	L15	400	0.08	120	0	1.17	1.16	1.15	
Irradiation test duct	F2-G2-G3	400	12.5	84	9	2.40	2.36	--	
Ionization chamber duct	13DS	360	53.0	118	15	0.40	0.37	0.38	

2. Measurement of neutron temperature and hyperthermal neutron flux

A lutetium-manganese plate was used to measure neutron temperature. The neutron temperature value T_n was obtained by comparing the activation of two types of nuclei in companion positions and the known pure thermal neutron spectrum after exposure. When the water temperature in the active section was 21°C, the measured value was $T_n = 479 \pm 35$ K.

Gold and manganese plates were used for measurements in the active section.

$$\frac{\Phi_{\text{epi}}}{\Phi_{\text{th}}} = 0.125 \pm 0.032$$

The Φ_{epi} in the formula is equal to the unit flux interval hyperthermal neutron flux. Φ_{th} is the hot neutron integral flux.

3. Measurement of neutron flux distribution

Nickel plate was used to measure the fast flux distribution in the entire reactor. The results of the experiment are shown in Table 10. The fast flux axial distribution of the J10 element box is shown in Figure 4. After the results of rapid spectral measurement were used to calculate the average

Table 10. Rapid Flux Distribution

Component	Position	Distance from reactor core (mm)	Height at maximum flux (mm)	Average sectional area of Ni58 (mb)	Reactor power (MW)	En>1MeV rapid flux ($\times 10^{11} \text{n/cm}^2/\text{s}$) h = 300 mm
Element	J10	64	250	123.0	0.08	7.2
Beryllium	P16	293	300	113.4	0.08	0.36
Temporary conduit	E11	384	300	99.4	0.08	0.096
Aluminum	C11	512	200	99.4	0.08	0.023

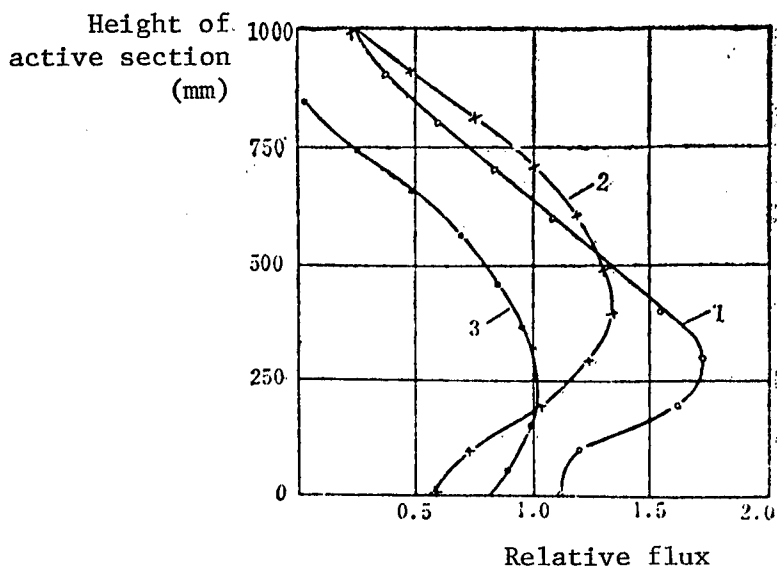


Figure 4. Axial Distribution of the Rapid and Thermal Neutron Flux in the J10 Element Box Position

Key:

1. Thermal flux distribution during the middle period of operation
2. Thermal flux distribution during the early period of operation
3. Rapid flux distribution during the early period of operation

cross section of the nickel, the absolute rapid flux value can be derived. The results shown in Table 9 are the final ones, and correspond well to the results of rapid spectral measurement.

VII. Measurement of Rapid Neutron Flux

1. Measurement of the relative distribution of the thermal flux of element boxes within the reactor

A manganese-nickel alloy plate was used to measure the thermal neutron flux. The detector plate was graduated relatively in the average thermal neutron field. Afterwards, the hot inlay method was used to inlay a 1,100 mm long, 8 mm wide and 1.5 mm thick polyvinyl bar. The detector bar was inserted into the water gap between each layer of elements to take the measurements. The water gap of the fuel pipe of the innermost layer (layer 1) was called the first layer water gap, and the others were numbered in sequence moving toward the outside. The number of detector plates in the water gap of each layer was 0, 1, 1, 2, 2, 3, 3. After exposure, the detector plates were measured in a semiautomatic sample exchanger device and were counted with a model DB-201D multichannel calibrator. The data was processed in a DJS-130.

Each detector bar provided an axial flux distribution. It was used to derive an average axial flux and an axial inconsistency coefficient (the axial inconsistency coefficient is defined as the ratio of the greatest flux to the average flux). The results of measurement of each detector plate in the water gaps of the same layer can be used to derive the average flux of that layer's water gap. The average flux of the element box can be derived by multiplying the average flux of each layer's water gap within an element by the water gap area factor. No measurements could be made in the water gap of the first layer because no detector plate was put in. Moreover, there is a difference between the flux of the water gap and that of the core. The average flux of the element boxes described above includes some error. The average flux of the entire reactor is derived by multiplying the average flux of each element box by the uranium content weight factor. The consistency coefficient of the entire reactor is the ratio between the maximum flux of the entire reactor and the average flux of the entire reactor.

The flux values of a portion of the element boxes in the active section during the early period of operation (the zero power experiment) are shown in Table 11. During the early and middle periods of operation (at the zero power stage, a portion of the elements around the outer portion were pulled out and the 1,2 SB were raised 265 mm). The axial flux distribution at the point of maximum flux is shown in Figure 4. See Table 12 for the results of measurements of the entire reactor. It can be seen from the results that the experimental average flux of the element boxes corresponds to the calculated value, with a 10 percent error range.

Element position	Average relative flux of box		Maximum relative flux of box	Nonuniformity coefficient of box
	Measured value	Calculated value		
H8	0.462	0.482	0.843	1.825
I9	0.762	0.691	1.098	1.441
J10	0.815	0.830	1.299	1.594
K8	0.438	0.402	0.683	1.559
K11	0.804	0.841	1.315	1.636

Table 12. Results of Flux Measurements of the Entire Reactor During the Early Period of Operation

<u>Parameter</u>	<u>Measured value</u>
Average flux of entire reactor	0.547 ± 0.006
Maximum flux	1.345 ± 0.042
Maximum flux position	Element box L12 in water gap of the number 7 layer, $H = 400$ mm
Single point absolute flux	$(7.18 \pm 0.43) \times 10^6$ n/cm ² /s

By using the method of least squares to fit the experimental flux points of the five central elements to a cosine function, the axial reflectivity layer reduction δ_h is:

$$\delta_h = 8.3 \pm 0.9 \text{ cm}$$

The construction method was used to derive the height of the central plane of the thermal flux of the active section h_0 as:

$$h_0 = 443 \pm 3 \text{ mm}$$

2. Absolute measurement of thermal neutron flux

Absolute measurements were made using the well-known gold leaf activation method, and counting was done using a model FH-424 $4\pi\beta-\gamma$ coincidence measurement device. It was derived after the results of the three types of reactor power levels were averaged. When measuring power with the ionization chamber placed in the 13DS duct and taking readings using a TR-84M read ammeter, the measured flux point nv_0 for each microampere was:

$$nv_0 = (2.47 \pm 0.12) \times 10^{10} \text{ n/cm}^2/\text{s}$$

VIII. Discussion of Results

A series of experimental data was obtained during the physical startup of the high flux reactor. This article provides various types of data on criticality and the absolute flux of fast and thermal neutrons corresponding to reactor power levels. There was a reasonable degree of correspondence between the theroretical calculations and experimental results in cold and thermal control rod efficiency, reactive reactor dynamics parameters, relative hot flux distribution, the distribution of gamma dose rates within the reactor and other parameters. Relative fast flux distribution, fast neutron energy spectrum and integral flux, reactivity coefficients and component reactivity and other parameters are first mainly being measured through experimentation.

Our work has shown that the reactivity measurement simulator is an easy to use and reliable instrument. The performance of several types of neutron measurement systems, multichannel calibrators and cross-correlation noise analyzers that were trial manufactured for this startup basically met demands. The predicted goal was achieved in the first application of the model DLS-204 reactor core gamma ionization chamber. The pulse neutron tubes, activation measurement plates and other equipment performed excellently. The use of these instruments and detectors meant that the physical startup could be easily completed in a fairly short period of time.

In simulator measurements, we put forth the method of temperature feedback correction and xenon poisoning correction in hot measurements.⁵ We successfully extrapolated criticality based on the control rod efficiency curve. The results of the experiment also show that in the area of control systems, the worrisome problem of the "blind section" can be overcome through highly sensitive measuring indicator gauges.

Measurements were made of the distribution of several physical parameters for the entire reactor. A great deal of work was completed. The experiments discovered that the planar height of the fast and thermal axial neutron flux in the active section were not the same. The geometric height of the center is 500 mm, the height of the hot flux center is 443 mm, while the height of the fast flux center is 300 mm. It is possible that these discrepancies are due to differences in the upper and lower reflection layers.

BIBLIOGRAPHY

1. Xu Chuanxiao [1776 0278 2400] et al., HE DONGLI GONGCHENG [NUCLEAR POWER ENGINEERING] Vol 2, No 3, p 1, 1981.
2. Xu Jiangqing [1776 3068 3237], et al., unpublished.
3. Peng Feng [1756 7685], "Several Types of Data Processing Procedures for Reactor Physical Testing," Report to the Second Nuclear Reactor Physics Conference of the Chinese Nuclear Society, Suzhou, 1980.
4. Fang Bangcheng, [2455 6721 2052], et al., unpublished.
5. Bu Yongxi [0592 3057 3556], et al., unpublished.

12539
CSO: 4008/97

APPLIED SCIENCES

EQUIPMENT FOR RECOVERY OF ENTRAINED ORGANIC MATTER FROM RAFFINATE IN SOLVENT EXTRACTION OF URANIUM

Beijing HE KEXUE YU GONGCHENG [CHINESE JOURNAL OF NUCLEAR SCIENCE AND ENGINEERING] in Chinese No 1, Mar 83 pp 36-43

[Article by Teng Yuanxun [3326 0337 8113] and Liu Min [0491 2404] of the Beijing Uranium Ore Processing Research Institute]

[Text] Abstract

The TPI tilted plate separator and follow-up coalescers are used to recover organic matter from the raffinate liquor in the solvent extraction of uranium with the result that the entrained organic matter can be reduced from 200-1,000 mg/l to ≤ 10 mg/l, the national standard for industrial discharge liquor, with a recovery efficiency of the entrained organic matter >90 percent. The results of experiments both in the laboratory and in industrial applications show that the above-mentioned equipment is of high efficiency and simple construction, and gives rapid separation of the organic matter with steady operation. Hence, the technical performance and economic indices are better and more advanced than those of conventional oil-water separators.

I. Preface

In the technical process of solvent extraction of uranium, the raffinate liquor contains some organic matter, usually from 200 to 1,000 mg/l. The primary organic matter is kerosene, so the goal of research on recovery equipment is to understand the question of oil and water separation.

In recent years, petroleum chemistry departments in China and abroad have developed several types of oil and water separation devices.¹ Some examples are the API level flow oil separation tank and the TPI tilted plate oil separation tank, which use the gravity separation method²; disk-plate centrifuges and centrifugal subsiders, which make use of centrifugal methods³; and integrated separation-filtration water and oil separators,⁴ tower-style adsorbers,⁵ vertical belt float oil and water separators,⁶ and horizontal coalescers, all using granularization methods.⁷

In the technical process of solvent extraction of uranium, the selection of oil and water separation equipment should be made in consideration of structural simplicity, ease of operation, low power consumption, high oil recovery efficiency, and ease of draining off sludge and floating oil. For this reason, we adopted the model TPI tilted plate separator⁸ and coalescer⁹ to process the organic material carried in the raffinate. Experimentation and industrial application has proven that this equipment is a small-scale, high-efficiency water and oil separation equipment for the recovery of organic matter in raffinate.

II. Technical Processes

The processed raffinate flows out of the extraction trough 1 into the water distribution pipe of the model TPI tilted plate oil separation equipment 2. It passes over the water distribution plate and then flows slowly and uniformly into the corrugated board group at a speed of less than 10 mm/sec. The oily water and sludge water are separated in the separation area. The oil droplets flow along the oil plate after separation and float to the water surface, while the solid floating matter is drained along the sludge plate into the sludge storage chamber. The organic matter that is recovered by the oil separation equipment is drained into the storage trough at fixed intervals by an oil skimming pipe. The raffinate containing the particulate oil after processing passes through a water outlet pipe at a fixed amount controlled by a model LZB-16 rotor flowmeter 4 into the coalescer 5. The granularization medium causes the micro-droplets of oil to gradually increase in size to the point where their buoyancy exceeds their weight, and they quickly float upward into the oil skimming cup. The waste water after processing is drained into a trench by the water drainage area, thereby completing the oil and water separation process. The flow chart is shown in Figure 1.

1. Structural design and experimental results of TPI tilted plate oil separation equipment.

The TPI tilted plate oil separation equipment that is currently being used in refining uranium water has a plate group arrangement of either a single plate group backflow or a double plate group backflow connected in parallel, as shown in Figure 2. The results of oil recovery are shown in Table 1.

It can be seen from Table 1 that TPI tilted plate oil separation equipment has excellent results and stable performance in the recovery of organic matter in raffinate.

- 1) The inlet area. The structural design of this area directly affects the results of oil recovery in the separation area. In order to make the liquid flowing into the separation area assume a laminar pattern, a stable flow energy dissipation device is installed at the inlet of the equipment.

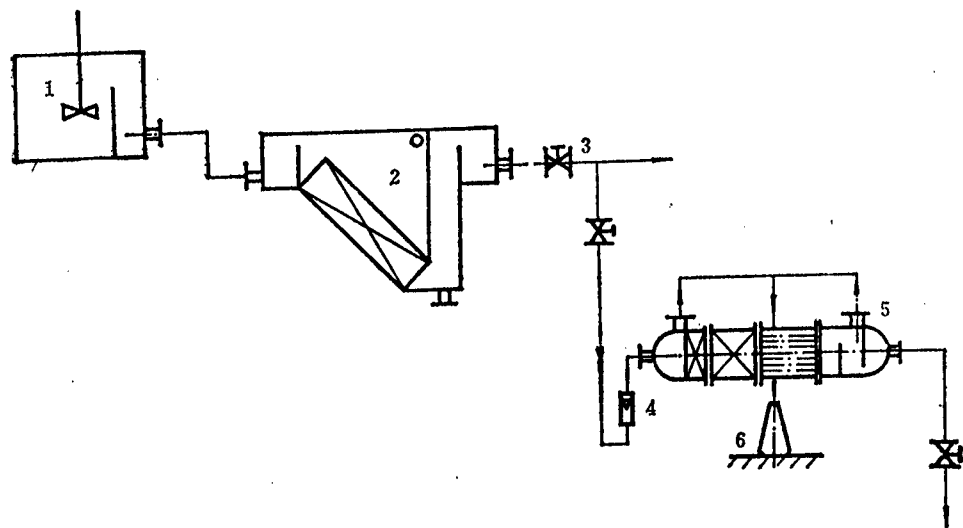


Figure 1. Technical Flowchart

Key:

1. Extraction trough	4. LZB-16 flowmeter
2. TPI tilted plate oil separation equipment	5. Coalescer
3. Valve	6. Oil skimming cup

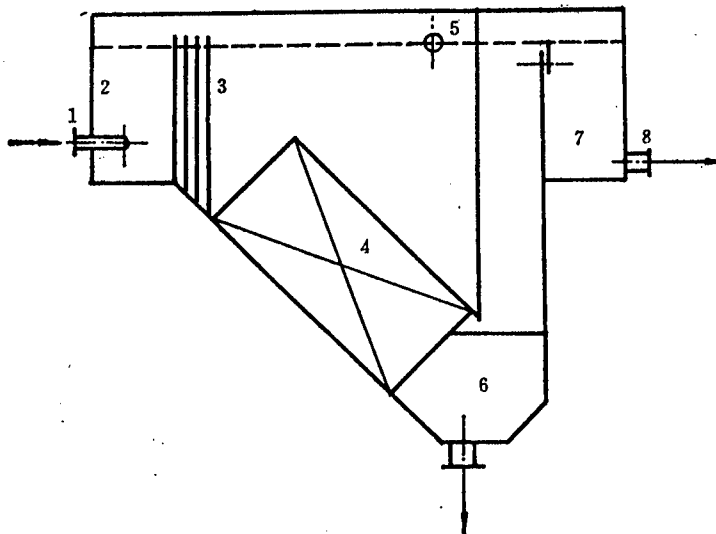


Figure 2. The 5 m³/h TPI Tilted Plate Oil Separation Equipment

Key:

1. Water intake pipe	5. Oil guide pipe
2. Water distribution chamber	6. Sludge chamber
3. Water distribution plate	7. Water outlet chamber
4. Corrugated plate group	8. Water drainage pipe

Table 1. Oil Recovery Results With 5 m³/h Equipment

Distance between plates (mm)	Organic material content at inlet (mg/l)			Organic material content at outlet (mg/l)			Effi- ciency (percent)
	Maximum value	Minimum value	Average value	Maximum value	Minimum value	Average value	
20	1,000	202	500	74	24	43	91.4
20	470	120	300	70	30	47	84.3
20	666	112	270	73	34	53	80.3

2) The water distribution area. In order to assure that the raffinate uniformly passes through each flow channel in the corrugated plate group, a water distribution plate is installed in the area to stabilize the distribution of the force of the water flow. The primary factor influencing the results of the overall flow of the water distribution plate is the rate of holes opened in the water distribution plate. Two standards, 20 percent and 30 percent, are used for the rate of holes opened in the TPI tilted plate oil separation equipment that has already gone into operation. The results are shown in Table 2.

Table 2. Open Hole Rate in the Water Distribution Plate and Oil Recovery Efficiency

	Open hole rate of 20 percent			Open hole rate of 30 percent		
	Organic material content at inlet (mg/l)	Organic material content at outlet (mg/l)	Effi- ciency (percent)	Organic material content at inlet (mg/l)	Organic material content at outlet (mg/l)	Effi- ciency (percent)
	353	23.3	93.4	377	16.3	95.7
	260	22.3	93.9	253	17.3	93.3
	255	18.5	92.5	286	19.3	93.4
Average value	385	16.5	95.6	283	23.0	91.8
	338	20.0	93.9	299	19.0	93.6

3) The transition zone. In order to cause the raffinate to form a laminar flow in the corrugated plate group, there is a suitable transition zone between the water distribution plate and the corrugated plate group. Its results were fairly good.

4) The oil-water, sludge-water separation zone. This is formed of a group of parallel corrugated plates, and is called the corrugated plate group.

a) The tilt angle of the corrugated plates: Experiments on the tilt angle were carried out to select a suitable angle of inclination. See Table 3 for the results.

Table 3. Tilt Angle of Corrugated Plates and Oil Recovery Efficiency

Tilt angle (degrees)	5	30	45	60
Flow rate (l/min)	0.125	0.125	0.125	0.125
Organic material content at outlet (mg/l)	56	75	80	133
Oil recovery efficiency	93.0	90.6	90.0	83.4

It can be seen from Table 3 that the smaller the tilt angle of the corrugated plates, the higher the oil recovery efficiency of the oil separation equipment. The recommended tilt angle of the plate group is 45°.

b) The space between the corrugated plates: the distances between the corrugated plates and the oil recovery efficiency are shown in Table 4.

Table 4. Distance Between Corrugated Plates and Oil Recovery Efficiency

Distance between plates (mm)	Organic material content at inlet (mg/l)			Organic material content at outlet (mg/l)			Effi- ciency (percent)
	Maximum value	Minimum value	Average value	Maximum value	Minimum value	Average value	
20	1,000	202	500	74	24	43	91.4
40	500	234	400	68	45	58	85.8
80	290	194	260	85	35	69	73.5

The design distance between plates was too small, however, causing an increase in the use of the corrugated plates. This led to an increase in the cost of capital construction and repairs. For raffinate liquor with a fairly high content of floating matter and sludge, it is best if the distance between the corrugated plates is not too small, in order to prevent the space between the plates from being blocked up by mud. It is best if the distance between the plates is from 20 to 40 mm.

c) The material used in the corrugated plates: The material selected for the corrugated plates in TPI inclined plate oil separation equipment is unsaturated polyester fiberglass.¹⁰ Its mechanical strength, technical performance and resistance to corrosion are fairly good, and contamination of the inclined plates can be overcome.

d) The shape of the inclined plates: The selection of the shape of the inclined plates must favor an increase in the surface area of the inclined plates and lower the surface load factor. The relationship between oil recovery efficiency and the surface load factor through the testing of TPI inclined plate oil separation equipment at 5 m³/h is shown in Table 5.

A corrugated shape was selected for the inclined plates in TPI inclined plate oil separation equipment, as shown in Figure 3.

Table 5. Surface Load Factor and Oil Recovery Efficiency

Surface load factor ($\times 10^{-4}$ m/s)	0.37	0.55	0.74	1.52	1.53	1.90	2.29
Organic material content at outlet (mg/l)	43	47	53	66	69	81	85
Oil recovery efficiency	91.4	84.3	80.3	78.0	73.5	76.8	71.5

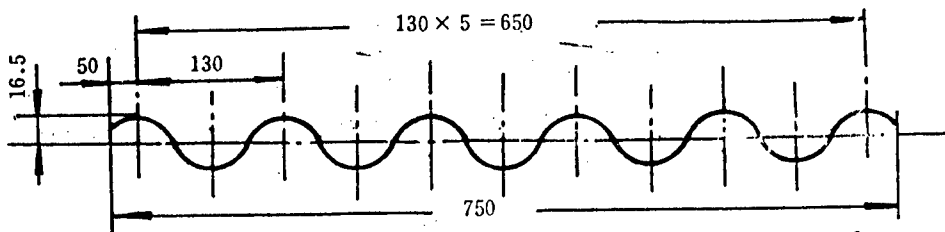


Figure 3. One Form of Corrugated Plate

e) The oil guide plate and sludge guide plate: The installation of an oil guide plate and sludge guide plate at the inlet and outlet ends of the corrugated board group can play a role in separating the flow of the oil, sludge and water, and can also fix the position of the corrugated plates and strengthen the rigidity of the plate group.

5) The oil collection area. The small droplets of oil carried in the raffinate are intercepted and coalesced by the tilted corrugated plate in the separation zone. After growing in size, they float upwards along the bottom surface of the corrugated plate. Oil drops larger than 50 μm in diameter float upward to the surface of the water due to the splitting by the oil guide plate. At this time, several bands of accumulated oil drops appear on the water surface. As time passes, the bands of oil collect to form an oil layer of a certain thickness. The oil layer is slowly drained into the oil skimming pipe as it flows forward along with the water current, thereby completing the oil recovery process.

6) The dirt region. Gravitational forces cause the solid particles that accumulate on the corrugated plate to slip downward into the channels on the corrugated plate. Gravity flow on the sludge guide plate continually drains them into the sludge chamber. In the liquid-liquid extraction process, the floating matter content on the raffinate liquor is generally less than 150 mg/l, and some is only about 20 mg/l. For this reason, it is best if the sludge storage chamber is not designed too large. To facilitate the draining of the sludge, the side walls of the sludge storage chamber should be designed to tilt at a 45° angle.

2. Structural design of the coalescer and test results

In order to more intensively deal with the raffinate containing microdroplets of oil that is drained out of TPI tilted plate oil separation equipment, we adopted the model PP-2 coalescer filled with polyacryl oil absorbing felt.¹¹ The structure of the equipment is shown in Figure 4.

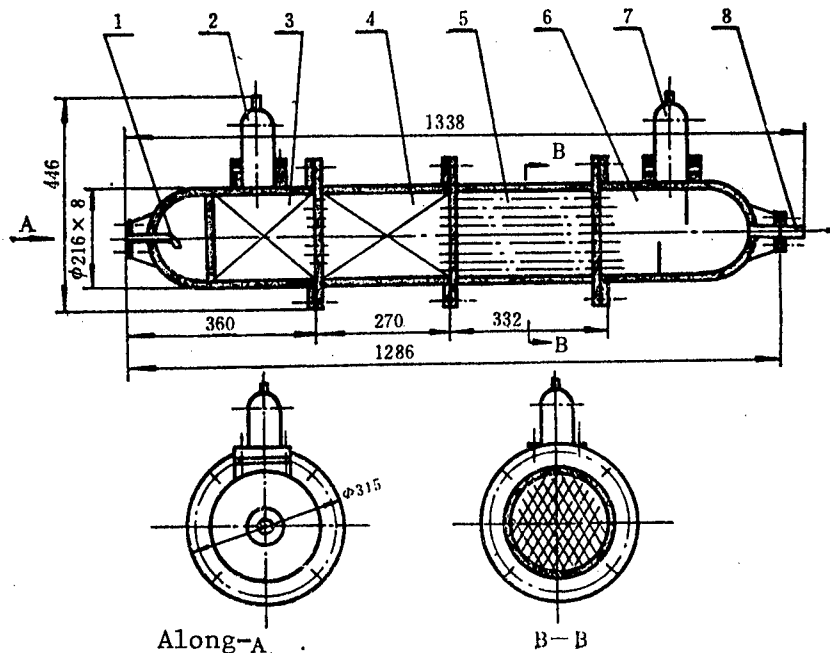


Figure 4. Coalescer Structure

Key:

1. Liquid inlet	5. Granularization area
2. Oil skimming cup	6. Water drainage area
3. Particle separation area	7. Oil skimming cup
4. Coalescence area	8. Water drainage outlet

1) The coarse separation area. This area is the preliminary processing stage. It first of all pulls in the large oil droplets in the materials liquid.

2) The coalescence area. This is the intensification processing stage. In order to intensify the coalescence of the small oil droplets, this area was filled with PP-2 polyacryl oil absorbing felt, glass wool and polyacryl beads.¹²⁻¹⁶ The results are shown in Table 6.

It can be seen from Table 6 that the oil recovery results of the coalescer are fairly good when using PP-2 polyacryl oil absorbing felt and glass wool as a granularization medium, while the results of the polyacryl beads are not ideal.

Table 6. The Influence of the Granularization Medium on Oil Recovery Efficiency

Fixation conditions	Granularization medium	Organic material content at inlet	Organic material content at outlet (mg/l)			Efficiency (percent)
		(mg/l)	Maximum value	Minimum value	Average value	
Entrained organic matter in raffinate is P-204 + TRPO + kerosene	PP-2 oil absorbing felt	61.4	11.0	7.5	8.8	84.8
	Glass wool	58.9	12.0	6.7	9.8	81.4
Entrained matter in raffinate is trilipoamine + mixed alcohol + kerosene	PP-2 oil absorbing felt	25.3	9.6	5.7	7.5	69.7
	Glass wool	26.5	10.1	3.0	7.3	71.5
	Polyacryl beads	23.1	11.5	2.6	8.3	64.2

It is best to use PP-2 polyacryl oil absorbing felt in coalescers used in industrial applications.¹⁷ Because the comparative surface area can be as high as 2,000 to 2,500 cm^2/g , the effective oil recovery area is large. After undergoing granularization in it, the diameter of the oil droplets can be 500 to 1,000 times greater than the original diameter. Moreover, the loss of water head in a coalescer filled with oil absorbing felt is only 20 mm of H_2O , while the loss of water head when using glass wool as a filler is as high as 60 to 80 mm of H_2O . The influences of the organic matter content in the raffinate on the oil recovery results when the filling density of the granularization medium is 0.145 g/cm^2 in the coalescer area are shown in Table 7.

3) The particle coalescence area. This is an auxiliary oil recovery stage. It traps the oil beads that were not recovered in the previous two areas of the oil droplets that leaked out, in order to reduce the content of organic matter at the coalescer outlet.

4) The water drainage area. This is a chamber for storage of the waste water after purification. The influence of changes in the length of the water drainage area on the results of oil recovery are shown in Table 8.

Table 7. The Influence of Organic Matter Content on Oil Recovery Efficiency

Fixation conditions	Organic matter content at inlet (mg/l)	Organic matter content at outlet (mg/l)			Efficiency (percent)
		Maximum value	Minimum value	Average value	
Entrained organic matter in raffinate is trilipo-amine + mixed alcohol + kerosene	10-20	6.0	2.8	4.1	68.3
	20-30	11.1	3.7	8.2	69.3
Entrained organic matter in raffinate is P-204 + TRPO + kerosene	30-50	10.5	5.0	7.3	84.6
	50-100	13.0	3.0	7.9	88.4
Entrained organic matter in raffinate is mixed alcohol + kerosene	300-10,000	31.5	13.8	20.1	99.6
	1,000-20,000	36.9	21.3	27.4	99.9

Table 8. The Influence of Changes in the Length of the Water Drainage Area on an Oil Recovery Efficiency

Structure	Length of water drainage area = 300 mm			Length of water drainage area = 540 mm		
	Maximum value	Minimum value	Average value	Maximum value	Minimum value	Average value
<u>Results:</u>						
	Effi-			Effi-		
1	80.4	11.0	48.2	7.0	8.5	81.4
2	87.3	11.0	54.2	8.0	9.0	88.2
Overall average value	83.9	11.0	51.0	7.5	8.8	84.8

III. Conclusion

1. TPI tilted plate oil separation equipment was used in series with a coalescer for processing trilipoamine and kerosene in the raffinate after uranium extraction. When the organic matter content of the processed raffinate is 200 to 1,000 mg/l, and when the surface load of TPI tilted plate oil separation equipment is 1×10^{-4} m/s, the organic matter content of the raffinate at the outlet of the equipment is 20 to 50 mg/l. After it passes through the coalescer, the organic matter content is reduced to 6-9 mg/l, with an average of 8 mg/l.

2. In the use of TPI tilted plate oil separation equipment in series with a coalescer for processing raffinate in which phosphorous solvents have been used to extract uranium, when the organic matter content of the processed raffinate liquor is 200 to 500 mg/l and the surface load factor of the TPI tilted plate oil separation equipment is 2×10^{-4} m/s, the organic matter content of the raffinate at the outlet of the equipment is 50 to 100 mg/l. After passing through the coalescer, the organic matter content dropped to 3 to 10 mg/l, with an average of 9 mg/l.

3. TPI tilted plate oil separation equipment has a large working surface area, a small upward floating distance, good water flow stability, ease in the downslide of mud, and other characteristics. Its utilization in series with the structurally simple, easy to operate coalescer filled with PP-2 polyacryl oil absorbing felt causes the organic matter content in the raffinate liquor to drop to the nationally-determined discharge standard of ≤ 10 mg/l.

4. Analysis of measurements by a model QGS-06 oil-bearing water analyzer meter and the results of microscopic observations and measurements show that the oil droplets in unprocessed raffinate are fairly large in diameter, the largest being 180 μm , and the smallest being about 20 μm . The characteristics of the distribution of oil droplets are that the large beads of oil have small oil droplets distributed around them in a circular distribution, as shown in Photograph 1 [omitted].

In the water discharged from TPI tilted plate oil separation equipment, the oil droplets are only 20 μm in diameter, with a few being 30 μm in diameter, as shown in Photograph 2 [omitted]. The oil droplets coming from the outlet of the coalescer are even smaller, all of them being less than 20 μm in diameter, as shown in Photograph 3 [omitted].

12539
CSO: 4008/97

APPLIED SCIENCE

NATION SAID TO RANK HIGH WITH 15 SATELLITES

OW050913 Beijing XINHUA in English 0803 GMT 5 Sep 84

["China Among Space Front-runners--21st of National Day Focus Series"--XINHUA headline]

[Text] Beijing, 5 Sep (XINHUA)--China has put 15 earth satellites into space in the past 15 years, and the latest, weighing over 900 kg, is still on course with all instruments functioning normally even though they have already fulfilled their mission.

A spokesman for the Astronautics Ministry said that this project shows that China ranks among the world's leading nations in carrier rocket and satellite technology.

The satellite was sent into space by a new type of carrier rocket on April 8 this year, along a trajectory the widest stretch of which is nearly 36,000 km. Within 8 days it was positioned 125 degrees east longitude above the earth's equator.

China started its astronautics industry in 1956 and launched its first carrier rocket in 1964. In May 1980, a carrier rocket was launched and recovered after splashdown in the destined areas. One year later, a single-launch vehicle sent three satellites into their respective orbits, and the following year China carried out a submarine-based carrier rocket launch.

With the development of rocket technology, China set about a program for launching man-made earth satellite from 1965. China's first satellite went into orbit in April 1970. It was followed by a scientific experiment satellite which sent back valuable data for 7 years circling the earth.

China is the third country in the world to master the technology for recovering satellites. A man-made satellite, launched in November 1975, returned to earth as scheduled after a 3-day flight. Since, then, four more satellites have been recovered.

A complete set of facilities have been built in the country for launching, monitoring and controlling rockets and satellites.

China's space technology is making great contributions to the national economy. Data collected by satellites have been successfully applied in land and forestry resources surveys, mineral exploration, hydrogeological prospecting and environmental monitoring.

APPLIED SCIENCES

REPORT ON NATIONAL TUNGSTEN-MOLYBDENUM CONFERENCE

Beijing GANGTIE [IRON AND STEEL] in Chinese No 10, 1983 p 69

[Article by Tang Xuwen [0781 4958 2429]: "National Tungsten-Molybdenum Conference"]

[Text] Under the leadership of the China Association of Sciences and Technology, the National Tungsten-Molybdenum Smelting and Processing Academic Society convened by the China Metals Society, the China Light Industry Association, and the China Electronics Society met in Tianjin in June, 1983.

The conference was attended by 110 representatives. At the meeting, 42 reports were presented dealing with processing of refractory materials, tungsten-molybdenum separation, refining, manufacture of blue [5691 5331] tungsten oxide, reduction of tungsten powder, pickling, research on doping methods and uniformity, new materials, jiapao [6905 3133] (Pauli's potassium?) theory and analytical testing.

In the discussion, the representatives felt that to realize the directive that Premier Zhou put forth when he was alive to turn around the situation of exporting tungsten ore and importing tungsten products. Since the first China Tungsten-Molybdenum Science and Technology [S&T] Forum in Shanghai in 1980, tungsten S&T work conferences have also been held in Xihuashan, Jiangxi, and Zhuzhou, Hunan. After the strategic mission of "vigorously developing the tungsten industry" was put forth, the S&T force of the tungsten-molybdenum world has been broadly mobilized and a series of technological attacks on key problems have been organized, making it possible to score achievements in smelting, selecting materials, processing, analysis and testing and applications. Because basic theoretical research on tungsten filaments has been strengthened, quality has improved and variety of products has been expanded so that tungsten filaments are in the main no longer imported. It has also brought about changes in the export makeup so that semifinished products and some finished products are exported.

During the discussions, representatives noted that at present we still fall short in industrial equipment, automation, and quality control as compared with advanced levels abroad. For this reason, the following proposals were put forth:

1. Carry out technological reform of existing production plants, constantly renew technology, adopt new industrial processes and new equipment. For this we should rely first on attacking technological key points and secondarily on importing advanced technology.
2. In importing technology, there should be careful research and importing should be from many countries, selecting the best of each.
3. Strengthen research on applying basic theory so that production technology can constantly advance.
4. New industrial processes and extending and applying the results of new technological research should be stressed and product standardization and seriation should be strengthened.
5. Planning and organizing cooperative work should be stressed in the hopes that relevant departments can early formulate a comprehensive plan of promoting the tungsten industry and developing the molybdenum industry, which includes tackling technological key areas, increasing their knowledge, and improving the export makeup.
6. It is hoped that the society can play an even greater role in developing its resourcefulness.

The representatives also proposed that the Third National Tungsten-Molybdenum S&T Conference be convened in 1985.

8226
CSO: 4008/83

APPLIED SCIENCES

PROTECTING CIVIL AIR DEFENSE INSTALLATIONS FROM SEEPAGE

Chongqing DIXIA GONGCHENG [UNDERGROUND ENGINEERING] in Chinese No 10, 1983
p 16

[Article by Liu Zhongyi [0491 1813 5030]: "Methods Used by the Shanhaiguan Bridge Girder Plant To Repair Seepage and Damp in Civil Air Defense Facilities"]

[Excerpt] For the past 10 years and more the Civil Air Defense Office of the Ministry of Railways' Shanhaiguan Bridge Girder Plant has built over 4,000 m² of civil air defense engineering projects, and except for a few reinforced concrete structures, they were primarily combination structures of brick and stone walls and reinforced concrete roofs and floors. Their height is 2-2.4 m, span 2-3 m, and earth cover 0.8-1.5 m. The plant is in a low-lying area which is in a sandy and gravelly alluvial belt so the ground water level is high, 1.5 m below the horizon water appears, thus the entire project is in the water. In the past, due to lack of civil air defense project design experience, quality of construction was deficient, leading to serious leaking in the project. In projects constructed before 1977 the water is 1.5 m or more deep yearround. Apart from surface seepage in brick and stone walls of composite structures, seepage is most prominent in seams between the walls and the ceiling and floor, lateral cracks, expansion joints, construction joints, changes in surface position, pipe holes in the walls, concrete honeycombing, and mouse holes. The reasons for this are: 1) when the brick walls of composite structures were laid up, low-quality mortar was used, only one layer of rigid waterproof covering was placed inside and out, construction quality was deficient, there were cavities, peeling, and cracks; 2) ordinary concrete was used, consistency was poor, and with the added deficiency in quality of construction there were problems with honeycombing, mouseholes, exposed reinforcing, and poor joints; 3) the gap in the expansion joints was too large, annular cracks appeared vertically, the quality of prefab expansion joints was poor, and the position of the water-stopping belt shifted; 4) during construction, open drains were used to carry off water, but measures were not vigorous enough, excavating was done with standing water, the ground was not level, water drained into the concrete, lowering its strength, and it settled unevenly; and 5) the positioning of conduits through the walls did not take waterproofing into consideration.

In view of the above situation, in 1978 ferric chloride waterproofing, "wuji" [0063 4335] waterproofing, and epoxy resin, cyanic coagulant, and

plastic coating were tried in an ongoing attempt to correct the situation depending on the different locations and characteristics of the seepage, achieving preliminary results in basically drying out the tunnels. After repair, things look quite different and some of the facilities are already being utilized.

8226
CSO: 4008/83

APPLIED SCIENCES

EXPERIMENTAL INVESTIGATION OF CRIPPLING STRENGTH OF CHINESE ALUMINUM ALLOY (LY12CZ) SECTIONS

Shanghai FUDAN XUEBAO-ZIRAN KEXUE BAN [FUDAN JOURNAL--NATURAL SCIENCES EDITION]
in Chinese No 4, 1983 pp 474-478

[Article* by Zhang Fubao [1728 4395 0202]: "Experimental Investigation of Crippling Strength of Chinese Aluminum Alloy LY12CZ Sections"]

[Text] Measurement of the crippling strength of aluminum alloy sections is very important for structural design in astronavigation. For this reason, we tested the crippling strength under axial pressure of 7 types of LY12CZ (Chinese Materials Standards) aluminum alloy sections, using 48 samples with 3 different effective slenderness ratios. In the end, we derived three semi-experimental formulas for calculating the crippling strength of domestically made aluminum alloy (LY12CZ) sections with an error range of \pm 10 percent. The formulas can be used in engineering design.

1. Test Goals and Samples

To provide design units with the semi-experimental formulas for the crippling strength of stiffened components, we selected samples from common, domestically produced aluminum alloy (LY12CZ) sections. The sections included equal-flanged angle stock, unequal-flanged unequal-thickness angle stock, bulbed-angle stock and T-shaped sections. These four types are extrusion sections. We also machined a type of Z-shaped sections from aluminum plate.

The sample lengths were determined according to the effective slenderness ratio. The basic standard was L/\sqrt{C} = 20. Some samples are longer, and some are shorter, within a range of about 5-10 cm. The C in the formula refers to the end face support coefficient. The value chosen here was C = 3^[1].

The processing requirements of the samples are as follows:

1. The non-parallelness of the samples' two end faces is 0.1;
2. The non-perpendicularity of the generating line to the end face of the samples is 0.15/100; and
3. The surface of each flange and web of the sample must be even.

*Paper received 6 March 1982.

To meet the above requirements, we first of all selected smooth samples, machined them and then did bench calibration tests. We tried to avoid using defective sections in order to increase the precision of the experiments.

2. Outline of the Experiment

This experiment used axial compression on the ends and demanded that there be no eccentric loading. Otherwise, the accuracy of the experimental results could be affected. For this reason, apart from using geometric comparison methods, we also placed resistance strain meters along the axis at symmetrical locations and in the corners. These are used to monitor eccentricity during the loading process. If the difference between sides corresponding to the increased strain from each step of increased loading (100 kg) is small, 30 micro-strains or less, this leads us to consider that the sample was physically centered.

After completing this preparatory work, we began formal loading. The corresponding strain value was recorded for each step of increased loading. These data were used to monitor the partial loss of stability in the sample. Partial loss of stability in the sample continued up to the instant where the sample could not continue bearing the load. At this time, the loading value indicated by the test instrument was equal to the crippling load of the sample. An unusual characteristic of the samples themselves was non-deformation of the generating line which was still maintained as a straight line, while the flanges and webs had already become distorted and lost stability by this time. In compression of an angle stock sample, for instance, its generating line was still a straight line, the included angle between the flanges was maintained as a right angle and the flange end section and its longitudinal side remained perpendicular. The edge of the flange did not remain a straight line, however, it became semi-wavelike instead. If there was obvious deformation of the sample's generating line, it was considered a total loss of stability and this load was not the crippling load. This experiment was done using an East German-made Model ZDM 5-ton mechanical and 30-ton-multipurpose-materials testing machine.

Strain measurements were made using a Model YJ-5 static electricity resistance gauge. The strain meter was a Model PZ-17 with a 2.8 X 15 mm paper base. The resistance value is 120 ohms \pm 0.3 ohms. The sensitivity coefficient $K = 2.02$. The strain meter was attached with Number 502 glue.

Figure 1 is an illustration of the typical position of the strain meters. The compressed-angle stock after crippling is shown in Figure 2.

3. Experimental Results and Analysis

We termed the damage in the sections that was caused by partial loss of stability "section crippling." The crippling strength was related to the shortness of the stock (an effective slenderness ratio of $L'/p \leq 20$). Within this range, strength obviously does not change along with the slenderness ratio.

Figure 1. Typical Positioning of Strain Meters

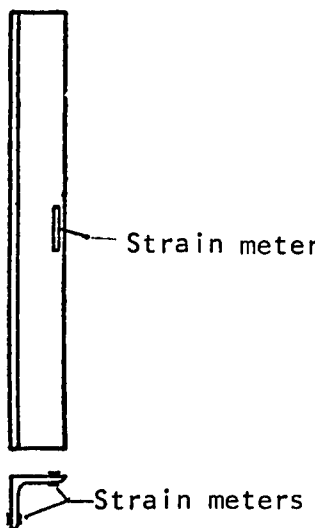


Figure 2. Compressed-angle Stock after Crippling



It was learned from generalized cropping analysis^[2-5] of a large amount of experimental data concerning the crippling strength of the sections that the crippling strength of the assigned material is determined by the geometric shape and special characteristics of the material as well as by the number of flanges or angles in the notch. This is shown in the formula below:

$$\frac{\sigma_f}{\sigma_{cy}} = \beta \left[\frac{qt^2}{A} \left(\frac{E}{\sigma_{cy}} \right)^{\frac{1}{3} \text{ or } \frac{1}{2}} \right]^m$$

where:

σ_f = crippling strength of the section,

σ_{cy} = compression yield strength of the material,

E = coefficient of elasticity of the material,

A = cross-sectional area of the section,

t = thickness,

g = coefficient related to the number of flanges or angles in the notch of the cross-section of the section, and

β = coefficient.

According to the results of this experiment, we did analysis and calculations of the crippling strength of three types of domestically made aluminum alloy

(LY12CZ) sections by applying regression analysis methods for processing the experimental data and using the semi-experimental analysis of others, and derived the following formulas:

1. Formula for crippling strength of compressed-corner stock:

$$\frac{\sigma_f}{\sigma_{0.2}} = 0.56 \left[\frac{2t^2}{A} \left(\frac{E}{\sigma_{0.2}} \right)^{\frac{1}{2}} \right] 0.85 .$$

2. Formula for crippling strength of compressed bulbed-corner stock:

$$\frac{\sigma_f}{\sigma_{0.2}} = 2.7 \left[\frac{t^2}{A} \left(\frac{E}{\sigma_{0.2}} \right)^{\frac{1}{3}} \right] 0.85 .$$

3. Formula for crippling strength of Z-shaped plate sections:

$$\frac{\sigma_f}{\sigma_{0.2}} = 3.3 \left[\frac{t^2}{A} \left(\frac{E}{\sigma_{0.2}} \right)^{\frac{1}{3}} \right] 0.75 .$$

The error between the calculated value and experimental value using the three formulas above is within ± 10 percent. A comparison of them is shown in Figures 3 to 5.

After comparing the above formulas with the formulas for the crippling strength of sections in Reference [2], we discovered that the two formulas were not completely identical. The coefficient in Formula 2, for instance, is 2.7, while Reference [2] uses 3.6. In addition, we substituted $\sigma_{0.2}$ for σ_{cy} , according to convention. The experimental value used for the special material characteristics in the calculations came from this experiment, and the experimental results have been used in engineering design.

This article was completed with major assistance from the Shanghai Machinery Plant. Qiu Ruiqiang [6726 3843 1730], Liang Guobao [2733 0948 1405], Zheng Guangping [6774 1684 1627], and other comrades also participated in the experiment.

REFERENCES

1. N. F. Dow, et. al., NACA, TN3064, 1954, 4.
2. G. Gerard, NACA, TN3784, 1957, 26.
3. E. F. Bruhu, "Analysis and Design of Flight Vehicle Structures," Ohio, 1965.
4. R. A. Needham, JOURNAL OF AERONAUTICAL SCIENCES, Vol 21, 1954, p 217.
5. Boeing Commercial Airplane Company, Boeing Designmanual (Section B Crippling), Seattle, 1973.

Table 1. Comparison of Test Values for the Crippling Strength of Sections and Values Calculated Using the Semi-exponential Formulas

Sample Number	Section Number	Test $\sigma_{0.2}$ (kg/cm ²)	Wall Thickness (cm)	Cross-Section Area A (cm ²)	Test E (kg/cm ³)	β	m	Test Strength $\sigma_{f, \text{test}}$ (kg/cm ²)	Test Strength $\sigma_{f, \text{cal}}$ (kg/cm ²)	Effective Length Ratio L'/ρ_{min}	Effective Length Ratio L'/ρ_{min}	Error $(\sigma_{f, \text{test}} - \sigma_{f, \text{cal}})/\sigma_{f, \text{test}}$
0200-01	XC111-16	3810	0.108	0.397	8.088×10^4	0.56	0.85	1870	1820	14.5	2.75%	
0200-02	XC111-16	3810	0.108	0.397	8.088×10^4	0.56	0.85	1870	1820	20.3	2.75%	
0200-04	XC114-4	3810	0.14 ⁽¹⁾	0.468	8.088×10^4	0.56	0.85	2620	2415	14.7	8.49%	
0200-05	XC114-4	3810	0.14	0.468	8.088×10^4	0.56	0.85	2620	2415	20.1	8.49%	
I-甲、乙、丙、丁	XC111-4	3810 ⁽¹⁾	0.113	0.294	8.088×10^4	0.56	0.85	2490	2572	19.4	-3.2%	
	XC141-10	3810	0.158	0.771	8.088×10^4	2.7	0.75	2910	2852	14.2	2.04%	
	XC141-10	3810	0.158	0.771	8.088×10^4	2.7	0.75	2910	2852	19.9	2.04%	
	XC141-12	3810	0.2	1.06	8.088×10^4	2.7	0.75	3250	3514	14.3	-7.6%	
0200-14	XC141-12	3810	0.2	1.06	8.088×10^4	2.7	0.75	3250	3514	19.5	-7.6%	
0200-15	XC411-4	2980	0.137	0.87	7.285×10^4	3.3	0.75	2180	2177	14.2	0.002%	
0200-17	XC411-4	2980	0.137	0.87	7.285×10^4	3.3	0.75	2180	2177	20	0.002%	
0200-18	XC411-4	2980	0.137	0.87	7.285×10^4	3.3	0.75	2260	2274	14.4	-0.62%	
0200-07	XC211-39	3810 ⁽¹⁾	0.207	1.468	8.088×10^4	0.64	0.40	2260	2274	20.4	-0.62%	
0200-08	XC211-39	3810	0.207	1.468	8.088×10^4	0.64	0.40					

Key:

a. Crippling strength σ_f calculated (kg/cm²)
b. Crippling strength σ_f tested (kg/cm²)
c. Effective slenderness ratio
d. Error: $(\sigma_f \text{ calculated} - \sigma_f \text{ tested})/\sigma_f \text{ tested}$

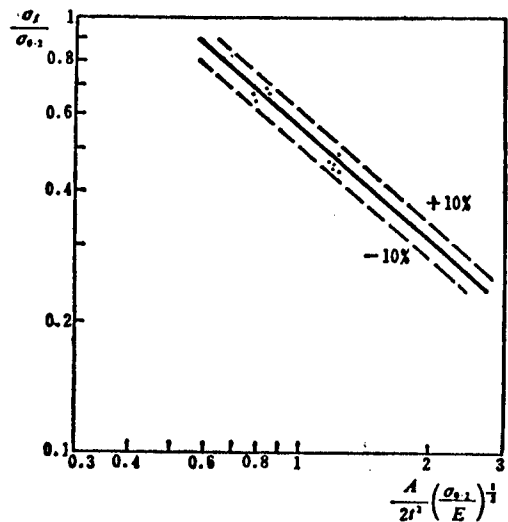
Notes: 1. $t = 0.14$ is the conversion value.
2. The mechanical properties of these two types of sections have not been measured, so the data for other types of sections were used.

3. In the effective slenderness ratio $L'/\rho_{\text{min}} = L/\sqrt{C} \rho_{\text{min}}$, the end support coefficient was 3 because flat-end compression was used.
4. The crippling strength of compressed T-shaped sections was calculated using the formula:

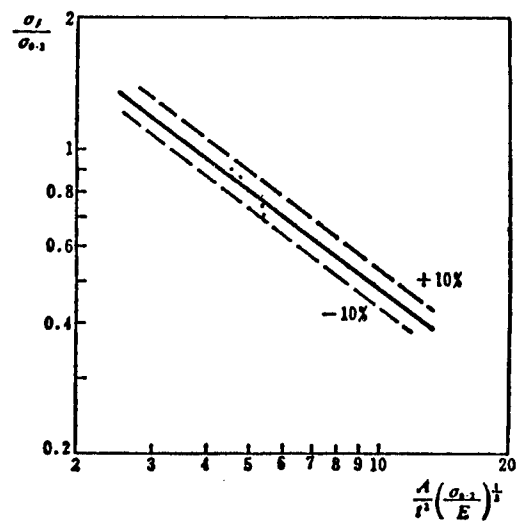
$$\sigma_f/\sigma_{f,0.2} = 0.54 \left[\frac{3t^2}{A} \left(\frac{E}{\sigma_{f,0.2}^2} \right) \frac{1}{2} \right]$$

Figures 3-5. Comparison of Error between Calculated Values and Test Values for Crippling Strength

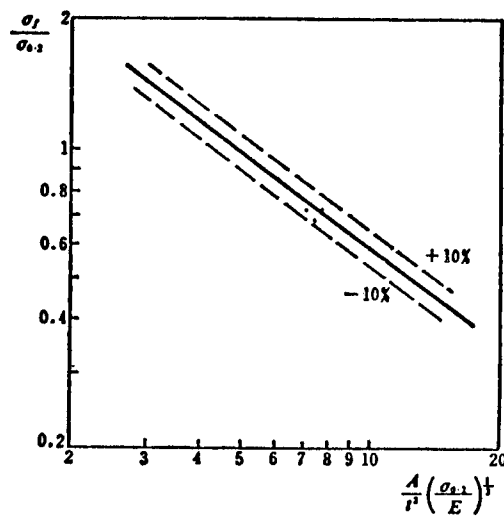
Compressed-corner Stock



Compressed Bulbed-corner Stock



Z-shaped Plate Sections



12539
CSO: 4008/137

APPLIED SCIENCES

INTERNATIONAL CONFERENCE ON RARE EARTH DEVELOPMENT AND APPLICATIONS AND INTERNATIONAL FAIR FOR RARE EARTHS AND THEIR APPLICATION PRODUCTS

Beijing ZHONGGUO XITU XUEBAO [JOURNAL OF THE CHINESE RARE EARTH SOCIETY] in Chinese No 1, 1984 pp 109-111

[Text] Beijing, China, 10-14 September 1985

In order to provide more opportunities for further academic discussions and technical cooperation among scientists, experts and industrialists from different areas of the world, it has been decided that on 10-14 September 1985 under the sponsorship of The Chinese Rare Earth Society, an International Conference on Rare Earth Development and Applications will be held in Beijing. Chairman of local committee of the Conference is Zhou Chuandian [0719 0278 0368], president of The Chinese Rare Earth Society. At the same time, another International Fair for Rare Earths and Their Application Products, sponsored by State Council for The Promotion of International Trade and The Chinese Rare Earth Society, will also be held here. Chairman of the local committee of the fair is Xu Chi [1776 7459], adviser of the State Economic Commission and leader of the Steering Group for the Promotion of Rare Earth Applications.

Topics Covered by the Conference

- A. Rare earth resources, geochemistry and ore dressing
- B. Rare earth applications in material science and engineering
 - 1. Luminescence and phosphors, lasers and spectroscopy, ligand field theory
 - 2. Magnetism and intermetallics
 - 3. Hydrogen storage materials
 - 4. Rare earth application in glasses and ceramics
- C. Rare earth applications in steel, cast iron and nonferrous metals.
 - 1. Metallurgical processing and method of addition
 - 2. Solidification, second phases and their shape control

- 3. Interaction with microalloying elements, impurities and hydrogen
- 4. Structure and properties
- 5. Rare earth in steel, such as HSLA, corrosion resistant, wear resistant and heat resistant steels, aluminum, other metals and their alloys
- 6. Rare earth containing modifiers and inoculants and their applications
- 7. Future developments and prospects

D. Rare earth chemistry and rare earth catalysis in petroleum and chemical industries

- 1. Solvent extraction chemistry and solution chemistry
- 2. Coordination chemistry and organometallic chemistry
- 3. Molten salt chemistry
- 4. Bioinorganic chemistry
- 5. Analytical chemistry
- 6. Structural chemistry, X-ray diffraction, IR and Raman spectroscopy NMR, ESCA etc.
- 7. Quantum chemistry

E. Rare earth production technology

- 1. Preparation of rare earth chloride
- 2. Solvent extraction processes
- 3. Ion exchange and chromatography
- 4. Preparation of rare earth metals and alloys
- 5. Other industrial processes
- 6. Environmental protection and toxicity

F. Other applications

- 1. Agricultural applications
- 2. Medical Applications
- 3. Wool dyeing and leather tanning
- 4. Miscellaneous applications

Items for Exhibition

- A. Rare earth research, production and application technologies for exchange or transfer
- B. Rare earth products
- C. Rare earth application products
- D. Reagent chemicals, instruments and equipment for use in research, production and applications

CSO: 4010/139

LIFE SCIENCES

BETTER FOOD, HEALTHCARE INCREASE AVERAGE SIZE

OW070921 Beijing XINHUA in English 0853 GMT 7 Sep 84

[Text] Beijing, 7 Sep (XINHUA)---Beijing men and women are the tallest and heaviest in China, and Beijing men have the biggest feet, according to a survey.

Youngsters in the capital are also the biggest, says the survey published in this week's edition of OUTLOOK magazine.

The average height of children all over China has been increasing by up to two centimeters a decade in the latter part of this century, said Cheng Mingda, deputy director of the Physical Culture Research Institute in Beijing.

Improved nutrition, medical health and sports facilities are regarded as the chief reasons for this.

The OUTLOOK survey of 16 provinces and cities shows that the average height of a Beijing man today is 172.7 cm, and a woman 161.2 cm.

Beijing men tip the scales at 61.7 kilograms on average, and women weigh 53.5 kilos. The prize for big feet goes to Beijing men with an average size of 25.2 cm. The women's average is 23 cm.

The smallest people surveyed were from Guangdong Province, where men's average height is 168.9 cm, women is 157.1 cm, and men weigh 55.8 kilos and women 49.1 kilos on average.

The size of feet has grown tremendously in the past 40 years.

Senior shop assistant at Lisheng sports goods store, the biggest in Beijing, said: "The biggest sport shoes we sold were size eight in the 1940's. But now there are a lot of youngsters demanding size 12 even size 13. Today, many women wear size seven shoes, but they chose size two in the '40's."

CSO: 4010/145

LIFE SCIENCES

BRIEFS

NEI MONGGOL MEDICAL CONFERENCE--The first work conference on medicine among national minorities, sponsored by the Ministry of Public Health and the State Nationalities Affairs Commission, opened in Hohhot, Nei Monggol, on 1 September. Attending and addressing the conference were Tan Yunhe, vice minister of public health; responsible persons of the relevant departments of the State Nationalities Affairs Commission; and Zhao Zhihong, vice chairman of the region. According to incomplete statistics, the country has some 3,700 professional medical personnel of minority nationalities and 130 state or collective hospitals and research units for minority medicine. Tan Yunhe spoke, calling for efforts to train medical personnel and work out plans for the development of medicine among national minorities. [Summary] [Hohhot Nei Monggol Regional Service in Mandarin 1100 GMT 1 Sep 84 SK]

CSO: 4003/407

ASTRONAUTICS

AUTHORS: PANG Cheng [7893 6134] and JIANG Weiqing [3068 3262 3237]

ORG: None

TITLE: "Study of Effective Physiological Temperature"

SOURCE: Beijing YUHANG XUEBAO [JOURNAL OF THE CHINESE SOCIETY OF ASTRONAUTICS] in Chinese No 2, 30 Apr 84 pp 10-15

ABSTRACT: The effect of temperature, humidity, and wind speed on the human body was studied under a variety of conditions. Experiments were conducted with 161 young men wearing 0.5C10 clothing in a high temperature cabin where microclimatic factors could be controlled in the following ranges: temperature 40-60°C, relative humidity 25-75 percent, wind speed 0.25-1.00 m/sec. The rates and magnitudes of changes in body temperature, heart beat rate, and perspiration were determined. It was discovered that each microclimatic factor does not affect the body independently. Instead, it is always related to other factors. The effect of wind speed is affected by temperature and humidity. When the temperature is higher than the body temperature, the wind speed has a heating effect due to convection. Otherwise, it has a cooling effect. When the ambient humidity is high, the heat dissipation effect is insignificant. In low humidity, the heat dissipation effect might cancel the convection heating effect at high temperatures. A mathematical expression was obtained based on the high temperature endurance data measured with 24 combinations of microclimatic factors. A nomogram of endurance time under various conditions was obtained. The effective physiological temperature diagram was prepared by finding various combinations of temperature, humidity, and wind speed with the same endurance time. It is a comprehensive and objective biological indicator for the engineering design and medical evaluation of the environmental control system in a space vehicle.

Comrades HUANG Rentao [7806 0086 3447] and XIANG Chengao [0686 2052 7559] participated in this work. The manuscript was received on 9 May 1983.

12553

CSO: 4009/98

ASTRONAUTICS

AUTHOR: SUN Shiqing [1327 0099 3237]

ORG: None

TITLE: "Space Interception Guidance with Uncertain Factors"

SOURCE: Beijing YUHANG XUEBAO [JOURNAL OF THE CHINESE SOCIETY OF ASTRONAUTICS] in Chinese No 2, 30 Apr 84 pp 32-42

ABSTRACT: Conventional methods are not applicable to the interception guidance of modern space vehicles traveling at extremely high speeds. A specific manifold was derived for space interception guidance with uncertain factors and arbitrary acceleration based on concepts of interception manifold and relative reference trajectory. It was analyzed from a differential viewpoint to provide rules for guidance. The equations of motion were simplified and integrated. The interception manifold was defined. The solutions to the high speed problem and the minimum energy problem were derived in detail. Furthermore, an example was given. The method significantly simplified the guidance process and was easy to execute. In a certain sense, it was a generalization of the conventional method.

The author wishes to thank SONG Jian [1345 1696] and HAN Jinqing [7281 0079 3237] for their valuable opinions. The manuscript was received on 9 May 1983.

12553

CSO: 4009/98

ASTRONAUTICS

AUTHORS: ZHANG Wei [1728 3555] and TIAN Deyu [3944 1795 0151]

ORG: None

TITLE: "Calculated Energetics of TN in Solid Propellants"

SOURCE: Beijing YUHANG XUEBAO [JOURNAL OF THE CHINESE SOCIETY OF ASTRONAUTICS] in Chinese No 2, 30 Apr 84 pp 84-90

ABSTRACT: The organic oxidizer 2,3,5,6-tetranitrato-1,4-dinitropiperazine (TN) was first synthesized by TIAN Deyu et al in the seventies. Its chemical formula was determined to be $C_4H_4N_8O_16$. The theoretical oxygen content is 60.95% and the volumetric oxygen content is 1.105 g/cm^3 , very close to that of liquid oxygen. As compared to ammonium perchlorate (Ap), it does not contain chlorine and has higher energy. The physicochemical properties of TN were discussed. The energetic characteristics of solid propellants such as HTPB-TN, HTPB-Al-TN, and HTPB-Al-Ap-TN, were calculated on a DPS-6 computer using a FORTRAN program based on White's Minimization of Gibbs Free Energy. The specific impulse I_{sp} of TN itself was found to be 233.21 sec. In 90% TN and 10% HTPB, the maximum specific impulse was 269.33 sec and the characteristic velocity (C^*) was 1610.5 m/sec. In the HTPB-TN-Al composite solid propellant system, I_{sp} and C^* could reach 276 sec, and 1662 m/sec, respectively. In the HTPB-Al-Tn-Ap system, when HTPB and Al were fixed, the specific impulse rose with increasing TN (Ap content was lowered correspondingly). It varied in the range from 265-275 sec. The energy of the propellant was increased by using TN as the oxidizer instead of Ap. Results indicated that TN is a promising replacement for Ap in smokeless propellants.

This manuscript was received on 21 July 1983.

12553

CSO: 4009/98

END